Exp. Theo. NANOTECHNOLOGY 10 (2026) 1027-1044 https://doi.org/10.56053/10.S.1027

Spray pyrolysis derived Ce-doped SnO_2 nanoparticles-based thin films: Tailoring band gap and conductivity for energy and optoelectronic applications

Ghassan E. Alkinani[1], *Abdul Rasool J. Katae*[2], *Mohammed RASHEED*[3,*]

[1]Ministry of Oil, Baghdad, Iraq
[2]Applied Sciences Department, University of Technology- Iraq, Baghdad 10066, Iraq
[3]College of Production Engineering & Metallurgy, University of Technology- Iraq, Baghdad, Iraq
[*]) Email: rasheed.mohammed40@yahoo.com

Received 28/1/2026, *Received in revised form* 26/3/2026, *Accepted* 17/4/2026, *Published* 15/5/2026

Ce-doped SnO_2 nanoparticle-based thin films with Ce concentrations of 0%, 1%, 3%, and 5% are successfully deposited on glass substrates using the spray pyrolysis method and systematically investigated for optoelectronic and sustainable energy applications. X-ray diffraction analysis confirmed that all films crystallize in the tetragonal rutile structure (JCPDS No. 41-1445) with space group $P4_2/mnm$, without any secondary phases, indicating successful incorporation of Ce into the SnO_2 lattice. The crystallite size decreased from ~26 nm to ~18 nm with increasing Ce content, accompanied by increased microstrain and dislocation density. FESEM and AFM analyses revealed a transition toward finer, more uniform, and compact nanoparticle morphology with reduced surface roughness (R_a decreased from 5.68 nm to 1.76 nm). Optical studies showed high transparency (~85–92%) in the visible region, with a slight decrease upon doping and a red shift of the absorption edge. The optical band gap, determined using Tauc plots, decreased from 3.85 eV for pure SnO_2 to 3.65 eV for SnO_2:Ce (5%), attributed to defect states and oxygen vacancies induced by Ce incorporation. FTIR spectra confirmed the presence of characteristic Sn–O bonds (~620–670 cm^{-1}) along with hydroxyl and adsorbed species, with slight variations due to doping. Hall effect measurements indicated a significant enhancement in electrical properties, with conductivity increasing from 55.56 to 238.10 $(\Omega \cdot cm)^{-1}$ and carrier concentration rising from 1.20×10^{20} to 3.60×10^{20} cm^{-3}. The maximum mobility (4.79 $cm^2.V^{-1}.s^{-1}$) is observed at 3% Ce, representing optimal doping. In general, SnO_2:Ce (3%) exhibited the best

combined structural, optical, and electrical performance, making it a promising candidate for advanced optoelectronic and energy applications.

Keywords: SnO_2 thin films; Cerium doping; Optoelectronic; Band gap.

1. INTRODUCTION

Tin oxide (SnO_2) is a wide-bandgap (≈3.6 eV) n-type semiconductor that has attracted significant attention due to its excellent optical transparency, high electrical conductivity, and remarkable chemical stability [1-5]. These properties make it a key material in various applications, including solar cells, gas sensors, photodetectors, and transparent conducting electrodes [6-10]. As a transparent conducting oxide (TCO), SnO_2 plays a vital role in sustainable energy technologies, particularly in photovoltaic systems, where it serves as a window layer allowing light transmission while maintaining electrical conduction [11-13]. Despite possessing some inherent properties that make it an effective optoelectronic material, intrinsic SnO_2 has a high resistivity that limits its use in optoelectronic devices [14-16]. The high resistivity of intrinsic SnO_2 results from a lack of sufficient charge carriers and defective sites caused by the presence of oxygen vacancies in the SnO2 crystal lattice [17-20]. Doping is an effective way to overcome the intrinsic limitations of SnO2 and many studies exist in this area demonstrating how to modify the structural, optical and electrical properties of SnO_2 using doping [21-25]. Doping SnO_2 with rare-earth (RE) elements has gained interest because of their unique electronic configurations which create defect states in the band structure of SnO_2 [26-30]. A RE element, cerium (Ce), is attractive as a dopant because it exists in two oxidation states (Ce3+/Ce4+) thus offering possibilities for charge compensation mechanisms and additional oxygen vacancies [31-35]. When SnO_2 is doped with Ce ions it adds some level of distortion to the lattice structure, whereas it will also increase its average grain size as well as the concentration of charge carriers. The effect of doping with Ce results in reduced optical band-gap and greater absorption of visible light and electrical conductance [41-45]. These effects will all play a role in enhancing the performance of both transparent conductors and energy converter devices [46-50]. The concentration of Ce used in the doping process is therefore critical to the overall performance of SnO_2 thin films. For example, when there is low Ce doping, the Ce ion may effectively replace the Sn4+ ion leading to greater crystallinity of the sample and increased electrical conductivity [51,52]. Therefore, the performance of SnO_2 thin films can be optimized only by matching the correct level of Ce doping, relative to optical transparency, electrical conductivity and structural integrity. Although a great deal of research has been done on doped SnO_2 thin films, there is still a significant lack of quantitative studies on the effect of different Ce concentrations on nanoparticle based SnO_2 thin films produced by sol-gel spray pyrolysis. This includes a lack of investigation into how the defects produced by Ce relate to the band gap tuning and electrical conductivity of the SnO_2 thin films. Historically, much of the research has been directed at either bulk materials or small ranges of doping concentration; as a result, there are gaps in our understanding of the optimal levels of doping that will yield good performing optoelectronic devices. There are a number of other issues in the literature pertaining to doped thin films of SnO_2, including the existence of non-uniform distributions of dopants, uncontrolled grain growth, and insufficient attention given to exploring defect-related optical properties, all of which will require carefully controlled syntheses and systematic characterization to better understand the structure-property relationship. The aim of this present investigation is to fabricate thin films consisting of SnO_2 nanoparticles with and without the addition of SnO_2. The films are fabricated using both 100% SnO_2 and 1%, 3%, and 5% Cedomo2-doped forms of SnO_2 using the spray pyrolysis method. The assessment of Ce-doped and un-doped samples with regard to their structure,

morphology, optics and electrical characteristics will take place in order to determine an ideal concentration of doping that maximizes the optoelectronic capabilities of the finished product. This study is unique because it establishes an inter-relation between the amount of Ce added and the effective size of the crystallites present in the thin film., band gap tuning, defect states, and electrical conductivity in nanoparticle-based thin films. Unlike previous studies, this research provides an integrated analysis linking microstructural modifications to optoelectronic behavior, offering deeper insight into the role of rare-earth doping in SnO_2 systems. In this paper, Ce-doped SnO_2 nanoparticle thin films are successfully prepared using the spray pyrolysis method, and their structural, optical, and electrical properties are systematically analyzed to evaluate their suitability for optoelectronic and sustainable energy applications.

2. MATERIALS AND METHODS

2.1. Thin film preparation

SnO_2 and Ce-doped SnO_2 (SnO_2:Ce) thin films with doping concentrations of 0%, 1%, 3%, and 5% are successfully deposited onto cleaned glass substrates using the spray pyrolysis technique. In this method, a precursor solution is prepared by dissolving an appropriate amount of tin (IV) chloride pentahydrate ($SnCl_4 \cdot 5H_2O$) in distilled water, followed by the addition of cerium nitrate hexahydrate ($Ce(NO_3)_3 \cdot 6H_2O$) as the dopant source according to the desired weight percentages. The solution is continuously stirred to obtain a clear and homogeneous mixture. Prior to deposition, glass substrates are ultrasonically cleaned using acetone, ethanol, and distilled water to remove surface contaminants. The precursor solution is then atomized into fine droplets using a spray nozzle and directed onto substrates heated at a temperature of 450 °C. Upon contact with the hot substrate, the droplets underwent thermal decomposition, resulting in the formation of SnO_2:Ce thin films. The deposition process is carried out for 15 minutes to achieve uniform film thickness. The key parameters such as spray rate, nozzle-to-substrate distance, and substrate temperature are carefully controlled to ensure good adhesion, uniformity, and reproducibility of the films. This technique offers advantages such as simplicity, low cost, scalability, and the ability to produce large-area coatings suitable for optoelectronic and energy-related applications. Figure 1 presents a schematic illustration of the preparation process of Ce-doped SnO_2 nanoparticle-based thin films using the spray pyrolysis method, highlighting the key steps including precursor solution preparation, spray deposition on a heated substrate, film formation, post-deposition annealing, and characterization [65,66].

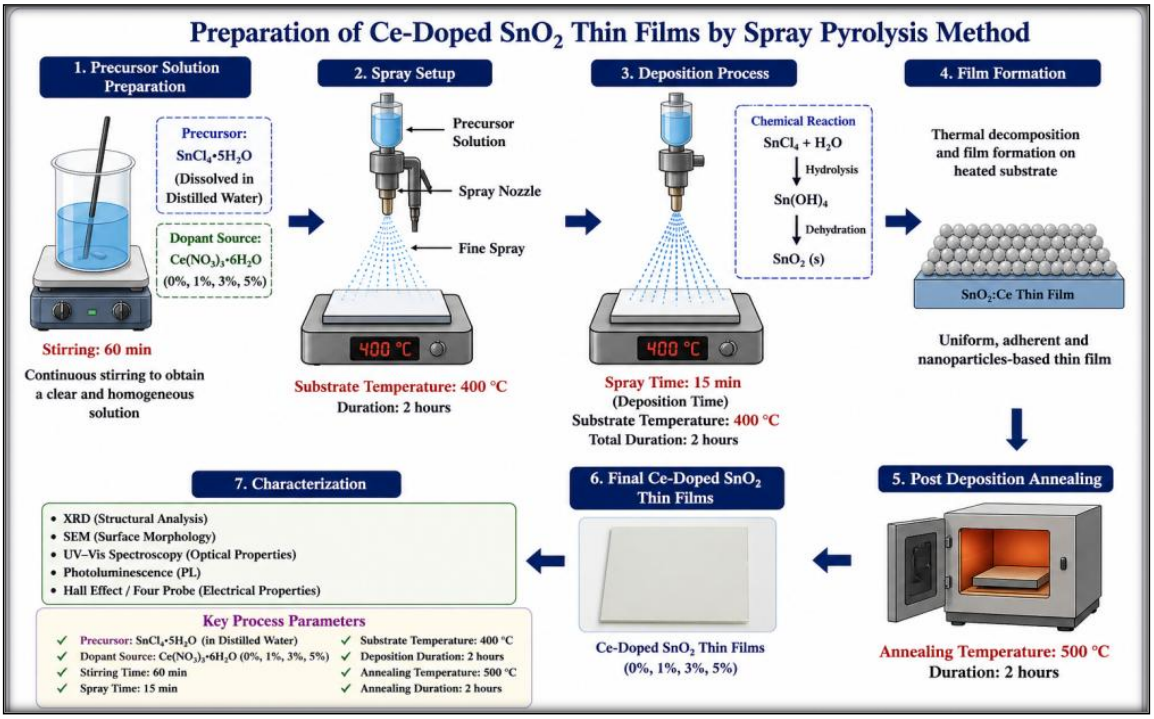

Figure 1 Schematic diagram of the spray pyrolysis process for the fabrication of Ce-doped SnO_2 nanoparticle-based thin films.

2.2. Characterization techniques

The structural properties of the prepared SnO_2 and Ce-doped SnO_2 thin films are analyzed using X-ray diffraction (XRD). The measurements are carried out using a Bruker D8 Advance X-ray Diffractometer (Bruker Corporation, Germany) equipped with Cu Kα radiation (λ = 1.5406 Å). The diffraction patterns are recorded over a 2θ range of 20° to 80° with a scanning step size of 0.02°. This technique is used to identify the crystalline phase, confirm the formation of tetragonal rutile SnO_2, and estimate the crystallite size using the Scherrer equation. Variations in peak intensity and broadening are analyzed to evaluate the influence of Ce doping on crystallinity and lattice distortion. Fourier Transform Infrared (FTIR) spectroscopy is employed to investigate the chemical bonding and functional groups present in the films. The spectra are recorded using a Thermo Scientific Nicolet iS10 FTIR Spectrometer (Thermo Fisher Scientific, USA) in the wavenumber range of 400–4000 cm^{-1}. FTIR analysis enabled the identification of Sn–O stretching vibrations and provided insights into the incorporation of Ce ions, as well as the presence of residual hydroxyl groups and possible precursor-related species. The surface morphology and elemental composition of the thin films are examined using scanning electron microscopy (SEM) coupled with energy dispersive X-ray spectroscopy (EDS). The measurements are performed using a FEI Quanta 250 FEG Scanning Electron Microscope (FEI Company, USA). SEM images at different magnifications are used to evaluate grain size, surface uniformity, and film compactness, while EDS analysis confirmed the elemental composition and successful incorporation of cerium into the SnO_2 lattice. In addition, the surface topography and roughness of the films are analyzed using atomic force microscopy (AFM). The measurements are performed using a Bruker Dimension Icon AFM system (Bruker Corporation, USA) operating in

tapping mode. The scans are recorded over an area of 5 μm × 5 μm to obtain both two-dimensional (2D) and three-dimensional (3D) surface images. AFM analysis provided quantitative information on surface roughness parameters, including average roughness (R_a) and root mean square roughness (R_{rms}), which are essential for understanding surface uniformity and its influence on optical and electrical properties. Optical properties of the films are studied using UV–Visible spectroscopy. The absorbance and transmittance spectra are measured using a Shimadzu UV-2600 UV–Vis Spectrophotometer (Shimadzu Corporation, Japan) in the wavelength range of 200–800 nm. The optical band gap is determined using Tauc plots derived from the absorption data. This analysis provided insight into the effect of Ce doping on optical transparency and band gap modulation, which are critical parameters for optoelectronic applications. The electrical properties of the thin films are evaluated using Hall effect measurements. The measurements are carried out using an Ecopia HMS-3000 Hall Measurement System (Ecopia Corporation, South Korea) under an applied magnetic field of 0.55 T. This technique allowed for the determination of key electrical parameters, including carrier concentration, Hall mobility, and resistivity. The Hall measurements provided a comprehensive understanding of charge transport mechanisms and the influence of Ce doping on the electrical performance of the SnO_2 thin films.

3. RESULTS AND DISCUSSION

3.1. Structural properties (XRD)

Figure 2 and Table 1 show the X-ray diffraction patterns of pure SnO_2 and Ce-doped SnO_2 thin films with Ce concentrations of 1%, 3%, and 5%. The observed diffraction peaks appear at approximately 2θ = 26.6°, 33.9°, 37.9°, 51.8°, and 54.7°, which correspond to the crystallographic planes (110), (101), (200), (211), and (220), respectively. These peaks confirm the formation of crystalline SnO_2 with a tetragonal rutile structure. The diffraction peaks are in good agreement with the standard SnO_2 reference pattern JCPDS card No. 41-1445. The crystal structure belongs to the tetragonal system with the space group $P4_2/mnm$ [67-70].

For tetragonal SnO_2, the lattice parameters are not equal in all directions; therefore, the correct relation is: $a = b \neq c$ with the interaxial angles: $\alpha = \beta = \gamma = 90^o$, the standard lattice parameters of rutile SnO_2 NPs thin films are: $a = b = 4.738\ A^{\circ}, c = 3.187\ A^{\circ}$, the absence of additional peaks related to CeO_2 or other impurity phases indicates that Ce ions are successfully incorporated into the SnO_2 lattice or existed below the detection limit of XRD. This confirms that Ce doping did not significantly alter the main tetragonal rutile structure of SnO_2. The crystallite size is calculated using the Scherrer equation: $D = \frac{K\lambda}{\beta cos\theta}$, where D is the crystallite size, K is the shape factor usually taken as 0.9, λ is the X-ray wavelength of CuKα radiation (1.5406 A˚), β is the full width at half maximum in radians, and θ is the Bragg diffraction angle [71,72].

Table 1 shows that the average crystallite size decreased from 26.0 nm for pure SnO_2 to 18.7 nm for SnO_2:Ce (5%). This decrease is attributed to the incorporation of Ce ions into the SnO_2 lattice, which creates lattice distortion and suppresses grain growth. The increase in FWHM with Ce concentration confirms peak broadening, indicating smaller crystallites and increased structural disorder. The d-spacing values are calculated using Bragg's law: $n\lambda = 2dsin\theta$, where n is the diffraction order, λ is the X-ray wavelength, d is the interplanar spacing, and θ is the diffraction angle. The calculated d-spacing values, such as 3.34 Å for the (110) plane and 2.64 Å for the (101) plane, agree well with the tetragonal SnO_2 phase. The microstrain is estimated using: $\varepsilon = \frac{\beta}{4tan\theta}$, the results show that microstrain increased from 5.5×10^{-3} for pure SnO_2 to 7.8×10^{-3} for SnO_2:Ce (5%). This increase indicates that Ce

doping introduces lattice defects and internal strain due to the ionic size difference between Sn and Ce ions. The dislocation density is calculated from: $\delta = \frac{1}{D^2}$, the dislocation density increased from 1.51 × 10^{15} m^{-2} for pure SnO_2 to 2.90 × 10^{15} m^{-2} for SnO_2:Ce (5%). This trend confirms that higher Ce doping generates more structural defects and grain boundaries. The peak intensity decreases gradually with increasing Ce concentration. This reduction can be attributed to reduced crystallinity, increased lattice disorder, and defect formation caused by Ce incorporation. However, the persistence of the main SnO_2 peaks confirms that all films retained the tetragonal rutile phase. Figure 2 and Table 1 confirm that Ce doping successfully modifies the structural properties of SnO_2 thin films by reducing crystallite size, increasing microstrain, and enhancing dislocation density, while maintaining the tetragonal rutile crystal structure [73-76].

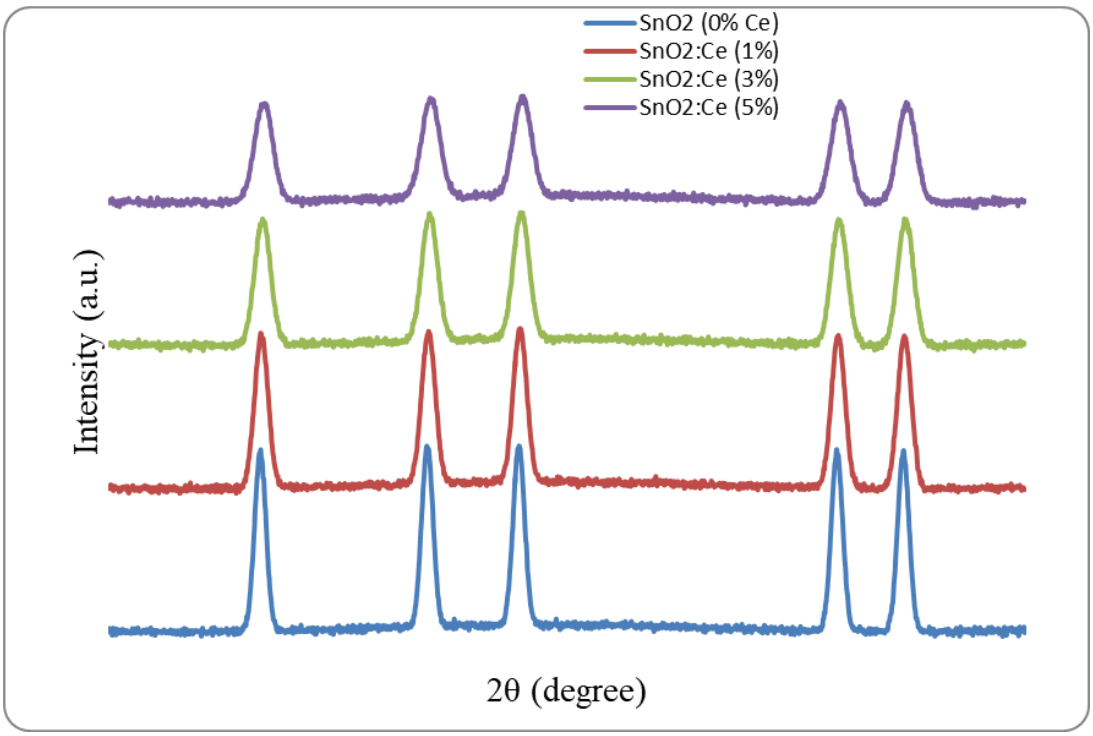

Figure 2 XRD patterns of SnO_2 and Ce-doped SnO_2 thin films with reduced peak intensities.

Table 1 XRD structural parameters of SnO_2 and SnO_2:Ce thin films.

Sample	**2θ (°)**	**(hkl)**	**FWHM (°)**	**d-spacing (Å)**	**D (nm)**	**ε ×10⁻³**	**δ ×10¹⁵ m⁻²**
SnO_2 (0% Ce)	26.60	(110)	0.28	3.34	29.5	4.7	1.15
	33.90	(101)	0.30	2.64	27.6	5.1	1.31
	37.90	(200)	0.32	2.37	25.8	5.5	1.50
	51.80	(211)	0.35	1.76	23.9	6.0	1.75
	54.70	(220)	0.36	1.67	23.2	6.2	1.85
Average	—	—	—	—	**26.0**	**5.5**	**1.51**
SnO_2:Ce (1%)	26.62	(110)	0.32	3.34	25.8	5.5	1.50
	33.92	(101)	0.34	2.64	24.3	5.9	1.69
	37.92	(200)	0.36	2.37	23.0	6.2	1.89
	51.82	(211)	0.38	1.76	21.8	6.6	2.10
	54.72	(220)	0.40	1.67	20.9	7.0	2.28
Average	—	—	—	—	**23.2**	**6.2**	**1.89**
SnO_2:Ce (3%)	26.65	(110)	0.36	3.34	23.0	6.2	1.89
	33.95	(101)	0.38	2.64	21.8	6.6	2.10
	37.95	(200)	0.40	2.37	20.9	7.0	2.28
	51.85	(211)	0.43	1.76	19.5	7.5	2.63
	54.75	(220)	0.45	1.67	18.6	7.8	2.88
Average	—	—	—	—	**20.8**	**7.0**	**2.36**
SnO_2:Ce (5%)	26.68	(110)	0.40	3.34	20.9	7.0	2.28
	33.98	(101)	0.42	2.64	19.9	7.4	2.52
	37.98	(200)	0.45	2.37	18.6	7.8	2.88
	51.88	(211)	0.48	1.76	17.5	8.3	3.26
	54.78	(220)	0.50	1.67	16.8	8.7	3.54
Average	—	—	—	—	**18.7**	**7.8**	

3.2.Morphological analysis (FESEM)

Figure 3 presents the field emission scanning electron microscopy (FESEM) images of SnO_2 and Ce-doped SnO_2 thin films prepared by the spray pyrolysis method with Ce concentrations of 0%, 1%, 3%, and 5%, along with their corresponding particle size distribution histograms (n = 250). The micrographs reveal that all samples exhibit a granular, nanoparticle-based morphology, which is typical for spray pyrolysis-grown oxide thin films. The surfaces are composed of closely packed, quasi-spherical nanoparticles with varying degrees of agglomeration depending on the dopant concentration. For the undoped SnO_2 film (Figure 3a), the surface shows relatively larger and loosely packed nanoparticles with noticeable agglomeration. The particles are quasi-spherical with an average size of approximately 82 ± 17 nm, as confirmed by the histogram. The broad distribution indicates non-uniform grain growth during deposition, which is characteristic of pure SnO_2 films due to the absence of dopant-induced nucleation control. The relatively larger grain size suggests enhanced grain coalescence during thermal decomposition at high substrate temperature. In the case of SnO_2:Ce (1%) (Figure 3b), the morphology becomes more uniform and compact, with a noticeable reduction in particle size to approximately 62 ± 13 nm. The distribution histogram becomes narrower, indicating improved homogeneity. The incorporation of Ce ions plays a significant role in modifying the

nucleation and growth mechanism, where Ce acts as a grain growth inhibitor, leading to finer particles and better surface coverage. The reduced agglomeration suggests improved film densification at this doping level. For the SnO_2:Ce (3%) film (Figure 3c), the surface exhibits highly uniform, densely packed nanoparticles with minimal voids and excellent surface coverage. The average particle size further decreases to approximately 47 ± 11 nm, and the histogram shows a relatively narrow and symmetric distribution. This indicates that 3% Ce doping represents an optimal concentration, where nucleation density is maximized, resulting in refined grain structure and enhanced film uniformity. The compact morphology is favorable for optoelectronic applications, as it can improve charge transport and reduce scattering at grain boundaries. At higher doping concentration, SnO_2:Ce (5%) (Figure 3d) shows ultrafine nanoparticles with an average size of approximately 36 ± 9 nm. Although the particles are significantly smaller, a slight increase in clustering or secondary agglomeration can be observed. This behavior is attributed to the excess Ce content, which introduces a high density of defects and localized strain, leading to partial particle coalescence. The distribution remains relatively narrow but slightly skewed, indicating increased structural disorder at higher dopant levels. The observed decrease in particle size with increasing Ce concentration is consistent with the crystallite size reduction obtained from XRD analysis (Table 1). This trend can be explained by the fact that Ce ions (Ce^{3+}/Ce^{4+}) introduce lattice distortion and inhibit grain boundary movement, thereby restricting crystal growth. Additionally, the presence of Ce enhances nucleation sites, leading to the formation of finer nanoparticles. The particle size distribution analysis (n = 250) for each sample confirms that Ce doping not only reduces the average particle size but also improves the uniformity of the films up to an optimal concentration (3%). Beyond this level, excessive doping leads to defect-induced clustering. The improved surface morphology and reduced particle size are expected to significantly enhance the surface-to-volume ratio, which is crucial for applications in gas sensing, photovoltaics, and optoelectronic devices. Figure 3 demonstrates that Ce doping effectively tailors the surface morphology of SnO_2 thin films by controlling nanoparticle size, distribution, and surface compactness, making these materials highly suitable for advanced energy and optoelectronic applications [77-79].

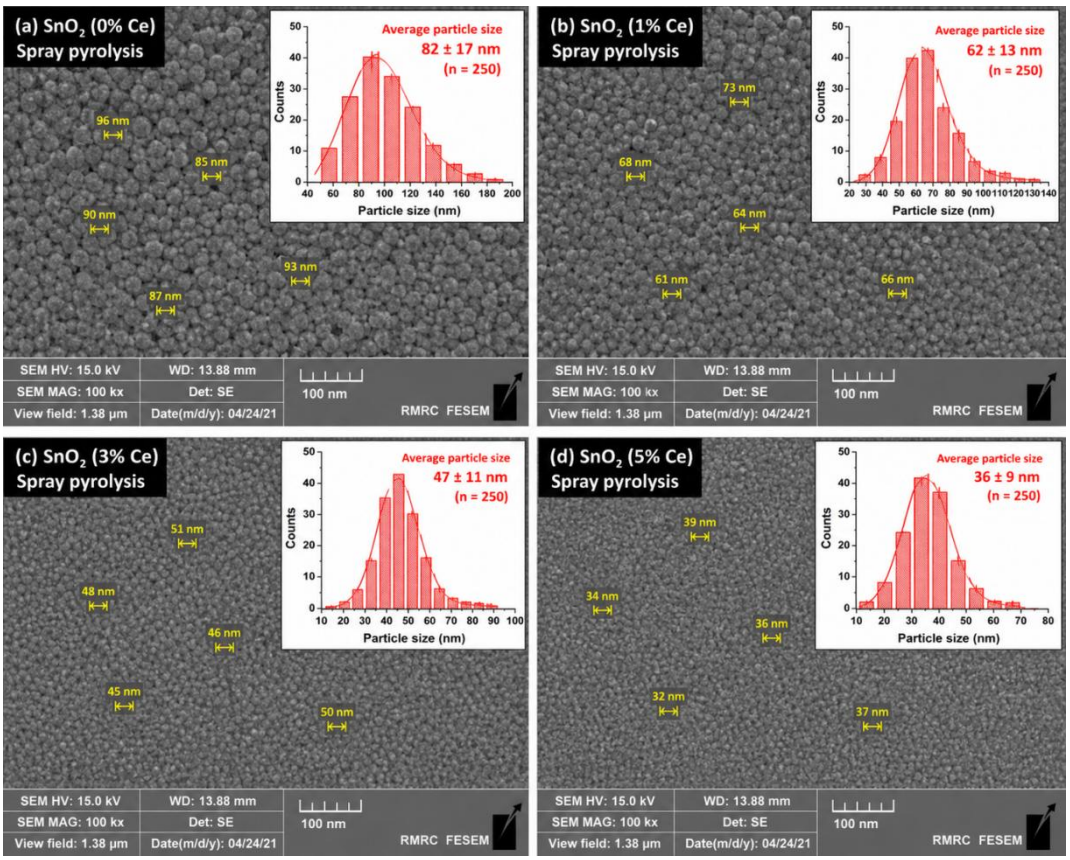

Figure 3 FESEM images of spray pyrolysis-deposited (a) SnO_2 (0% Ce), (b) SnO_2:Ce (1%), (c) SnO_2:Ce (3%), and (d) SnO_2:Ce (5%) thin films

3.3. AFM analysis

Figure 4 illustrates the two-dimensional (2D) and three-dimensional (3D) atomic force microscopy (AFM) images of SnO_2 and Ce-doped SnO_2 thin films prepared by the spray pyrolysis method with varying Ce concentrations (0%, 1%, 3%, and 5%). The scans are recorded over an area of 5 µm × 5 µm in tapping mode, providing detailed insight into the surface morphology, grain distribution, and roughness evolution as a function of Ce doping. The undoped SnO_2 film (Figure 4a) exhibits a relatively rough surface characterized by large, irregularly distributed grains and pronounced height variations. The 2D image shows bright regions corresponding to elevated grains, while the 3D topography confirms the presence of high peaks and deep valleys across the surface. This rough morphology is quantitatively supported by the higher roughness values ($R_a \approx 5.68$ nm and $R_{rms} \approx 7.21$ nm, Table 2), indicating significant surface irregularity. The larger grain size observed here is consistent with the FESEM and XRD results, where grain growth is less restricted in the absence of dopant ions. Upon introducing 1% Ce doping (Figure 4b), the surface becomes noticeably more uniform and smoother. The grains appear finer and more evenly distributed, leading to reduced height fluctuations. The 3D image shows a decrease in peak-to-valley contrast compared to the undoped sample. This improvement is reflected in the reduced roughness values ($R_a \approx 3.92$ nm and $R_{rms} \approx 4.98$ nm). The presence of Ce ions likely enhances nucleation density and suppresses excessive grain growth, resulting in a more compact and homogeneous film. For the SnO_2:Ce (3%) sample (Figure 4c),

the surface morphology reaches an optimal state, exhibiting high uniformity and dense grain packing. The grains are significantly smaller and more closely packed, forming a continuous and smooth film with minimal voids. The 3D topography shows a relatively flat surface with reduced height variation. Correspondingly, the roughness further decreases to $R_a \approx 2.48$ nm and $R_{rms} \approx 3.12$ nm, indicating improved surface smoothness. This suggests that 3% Ce doping provides the best balance between nucleation and growth, leading to refined microstructure and enhanced film quality. At higher doping levels, SnO_2:Ce (5%) (Figure 4d) demonstrates a surface composed of ultrafine grains with very low roughness. The 2D image appears highly compact with minimal contrast, and the 3D representation shows a nearly flat surface with very small height fluctuations. The roughness values decrease further to $R_a \approx 1.76$ nm and $R_{rms} \approx 2.25$ nm, confirming a highly smooth surface. However, although the surface appears smoother, excessive Ce incorporation may introduce structural defects and localized strain, which could affect other properties such as electrical conductivity. A clear trend is observed across all samples: increasing Ce concentration leads to a systematic reduction in surface roughness and grain size. This behavior is attributed to the role of Ce ions in modifying the growth kinetics of SnO_2 films. Specifically, Ce acts as a grain growth inhibitor by introducing lattice distortion and increasing nucleation sites, which results in finer grains and smoother surfaces. The reduction in roughness from Ra = 5.68 nm (0% Ce) to 1.76 nm (5% Ce) demonstrates a significant improvement in film smoothness. Similarly, the decrease in Rrms values indicates reduced surface height fluctuations and improved homogeneity. The most notable improvement in uniformity occurs at 3% Ce, where the films exhibit optimal surface morphology with balanced grain refinement and minimal defects. From an application perspective, smoother and more uniform surfaces are highly desirable for optoelectronic and energy devices, as they reduce light scattering, enhance charge transport, and improve interface quality. Therefore, the AFM results confirm that Ce doping effectively tailors the surface topography of SnO_2 thin films, with 3% Ce emerging as the optimal doping concentration for achieving high-quality films with superior surface characteristics [30,31].

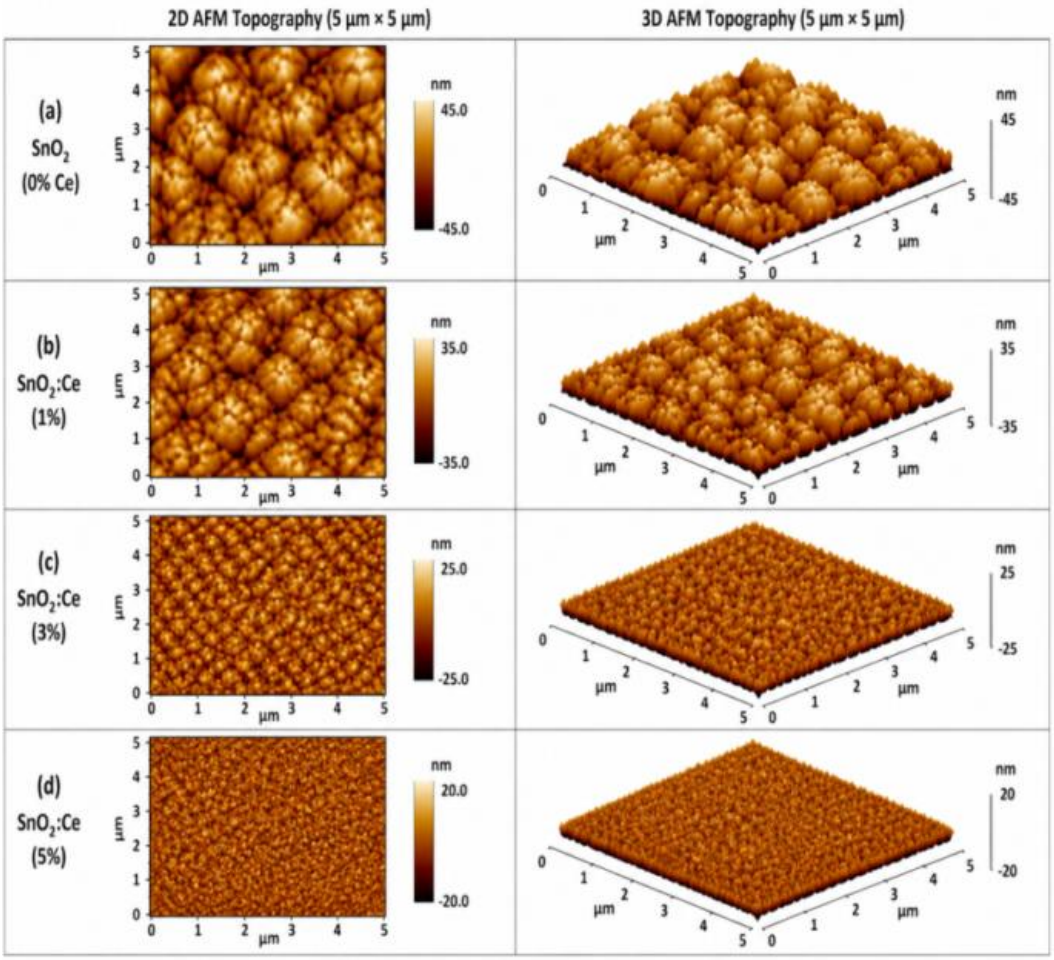

Figure 4 2D and 3D AFM topography images of spray pyrolysis-deposited (a) SnO_2 (0% Ce), (b) SnO_2:Ce (1%), (c) SnO_2:Ce (3%), and (d) SnO_2:Ce (5%) thin films scanned over an area of 5 µm × 5 µm in tapping mode.

Table 2 AFM roughness parameters of SnO_2 and SnO_2:Ce thin films.

Sample	R_a (nm)	R_{rms} (nm)
SnO_2 (0% Ce)	5.68	7.21
SnO_2:Ce (1%)	3.92	4.98
SnO_2:Ce (3%)	2.48	3.12
SnO_2:Ce (5%)	1.76	2.25

Figure 5 shows the optical transmittance spectra of SnO_2 and Ce-doped SnO_2 thin films in the wavelength range of 300–900 nm. All samples exhibit high optical transparency in the visible region, confirming that the prepared films are suitable for transparent optoelectronic and energy-related applications. The undoped SnO_2 film shows the highest transmittance, reaching approximately 90% in the visible region. With increasing Ce concentration, a slight decrease in transmittance is observed. The transmittance decreases in the order: SnO_2>SnO_2:Ce (1%)>SnO_2:Ce (3%)>SnO_2:Ce (5%). This

reduction may be attributed to increased light scattering and absorption caused by Ce incorporation, defect formation, and oxygen vacancies. The presence of Ce ions can introduce localized defect states within the band structure, which enhance optical absorption and slightly reduce transparency. The spectra also show a sharp increase in transmittance near the ultraviolet–visible region, indicating the absorption edge of SnO_2-based thin films. With Ce doping, the absorption edge shifts slightly toward longer wavelengths. This red shift suggests a narrowing of the optical band gap, which is commonly associated with dopant-induced defect levels and structural disorder. The high transmittance values, especially above 400 nm, indicate that the films maintain good optical transparency despite Ce incorporation. This is important for transparent conducting oxide applications, where both transparency and electrical conductivity are required. Among the doped samples, SnO_2:Ce (3%) provides a good balance between high transmittance and expected improved electrical performance, making it a suitable candidate for optoelectronic and sustainable energy devices [40-43].

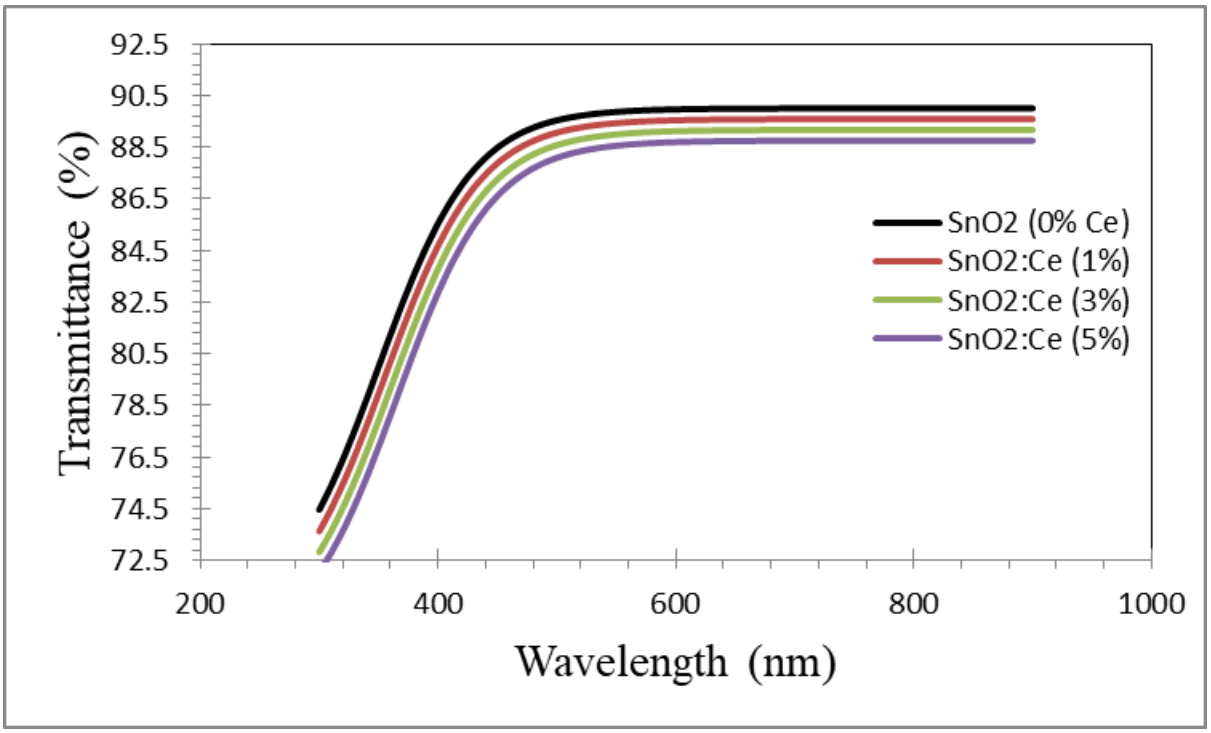

Figure 5 Optical transmittance spectra of spray pyrolysis-deposited SnO_2 (0% Ce) and Ce-doped SnO_2 thin films (1%, 3%, and 5%) measured in the wavelength range of 300–900 nm.

Figure 6 presents the Tauc plots of $(\alpha h\nu)^2$ as a function of photon energy $(h\nu)$ for SnO_2 and Ce-doped SnO_2 thin films (0%, 1%, 3%, and 5%). The plots are used to determine the optical band gap energy (E_g) based on the direct allowed electronic transition in SnO_2. All curves exhibit a characteristic behavior where $(\alpha h\nu)^2$ increases sharply near the absorption edge, indicating strong optical absorption and confirming the semiconducting nature of the films. The optical band gap is evaluated using the Tauc relation [44,45]:

$$(\alpha h\nu)^2 = A(h\nu - Eg) \quad (1)$$

where α is the absorption coefficient, $h\nu$ is the photon energy, A is a constant, and E_g is the optical band gap. For a direct allowed transition, the exponent is equal to 2. The band gap energy is obtained by extrapolating the linear region of each curve to the photon energy axis, i.e., where $(\alpha h\nu)^2 = 0$. From Figure 6, it is evident that the extrapolated intercepts shift toward lower photon energy values with increasing Ce concentration. The calculated band gap values are approximately 3.85 eV for SnO_2 (0% Ce), 3.78 eV for SnO_2:Ce (1%), 3.70 eV for SnO_2:Ce (3%), and 3.65 eV for SnO_2:Ce (5%). This systematic decrease in band gap energy indicates a clear band gap narrowing effect induced by Ce doping. The reduction in E_g can be attributed to several factors. The incorporation of Ce ions (Ce^{3+}/Ce^{4+}) into the SnO_2 lattice introduces localized defect states within the band gap, which facilitate electronic transitions at lower photon energies. Additionally, Ce doping enhances the formation of oxygen vacancies, which act as donor states and contribute to band tailing. This effect can be explained by the Urbach tail phenomenon, where the absorption edge becomes less abrupt due to increased structural disorder. Furthermore, the decrease in band gap may also be influenced by the interaction between Ce 4f orbitals and the conduction band of SnO_2, leading to the formation of intermediate energy levels. As the Ce concentration increases, these defect states become more pronounced, resulting in a gradual shift of the absorption edge toward longer wavelengths (red shift), which is consistent with the optical transmittance results discussed earlier. A comparative analysis of all samples reveals that the undoped SnO_2 film exhibits the widest band gap, indicating fewer defect states and a more intrinsic semiconductor behavior. In contrast, the doped films show progressively reduced band gaps, with the SnO_2:Ce (5%) sample exhibiting the lowest E_g due to the highest level of structural disorder and defect density. However, while higher doping enhances light absorption, excessive Ce incorporation may introduce recombination centers that can negatively affect device performance. Among all samples, the SnO_2:Ce (3%) film represents an optimal balance, offering a moderately reduced band gap while maintaining relatively good structural and optical properties. This makes it particularly suitable for applications in photovoltaics, photodetectors, and other optoelectronic devices, where enhanced visible light absorption is desirable [12,23].

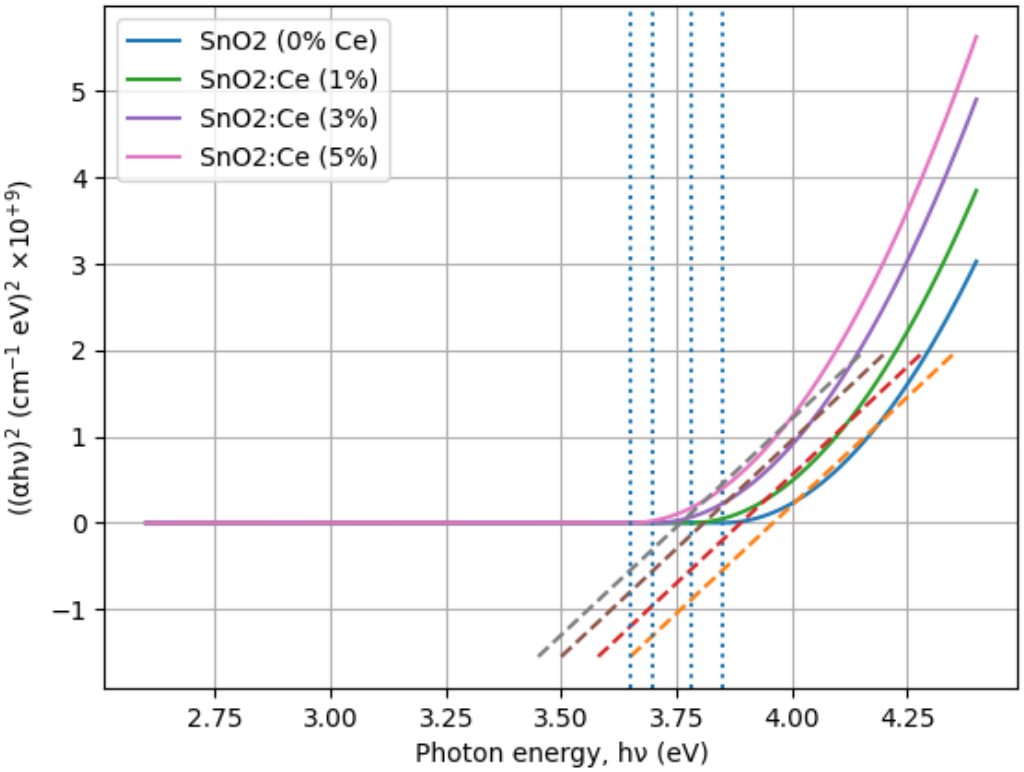

Figure 6 Tauc plots of $(\alpha h\nu)^2$ versus photon energy $(h\nu)$ for SnO_2 (0% Ce) and Ce-doped SnO_2 thin films (1%, 3%, and 5%)

Table 3 Optical band gap (E_g) values of SnO_2 and Ce-doped SnO_2 thin films determined from Tauc plots $(\alpha h\nu)^2$ versus $h\nu$. A systematic decrease in band gap with increasing Ce concentration is observed.

Sample	E_g (eV)
SnO_2 (0% Ce)	3.85
SnO_2:Ce (1%)	3.78
SnO_2:Ce (3%)	3.70
SnO_2:Ce (5%)	3.65

3.4.FTIR analysis

Figure 7 presents the FTIR spectra of SnO_2 and Ce-doped SnO_2 thin films with Ce concentrations of 1%, 3%, and 5%. The spectra show similar absorption bands for all samples, indicating that Ce incorporation does not significantly change the basic chemical bonding structure of SnO_2. However, slight changes in peak position and intensity are observed with increasing Ce concentration, confirming the influence of Ce doping on bonding environment and defect formation. The strong absorption band observed around 620–670 cm^{-1} is attributed to the stretching vibration of the Sn–O–Sn / Sn–O bond, confirming the formation of SnO_2. A slight shift of this band with Ce doping indicates

lattice distortion caused by the incorporation of Ce ions into the SnO_2 matrix. This behavior is consistent with the XRD results, where peak broadening and increased strain are observed with increasing Ce content. The band around 1400–1450 cm^{-1} may be assigned to residual nitrate-related vibrations or surface adsorbed species originating from the precursor salts. The intensity of this band changes slightly with Ce concentration, suggesting variation in residual surface groups and film densification after annealing. The absorption peak near 1600–1650 cm^{-1} corresponds to the bending vibration of adsorbed water molecules or hydroxyl groups (H–O–H), while the broad band around 3300–3500 cm^{-1} is associated with O–H stretching vibrations from adsorbed moisture or surface hydroxyl groups. Comparatively, the undoped SnO_2 film exhibits more intense absorption features, especially in the O–H and Sn–O regions, indicating a higher amount of surface hydroxyl groups and larger grains. With increasing Ce concentration, slight changes in intensity and broadening are observed, which may be due to enhanced oxygen vacancy formation and modification of the local bonding environment. The spectra of SnO_2:Ce (3%) and SnO_2:Ce (5%) remain similar to the undoped film, confirming that the tetragonal SnO_2 network is preserved after Ce doping [25-27].

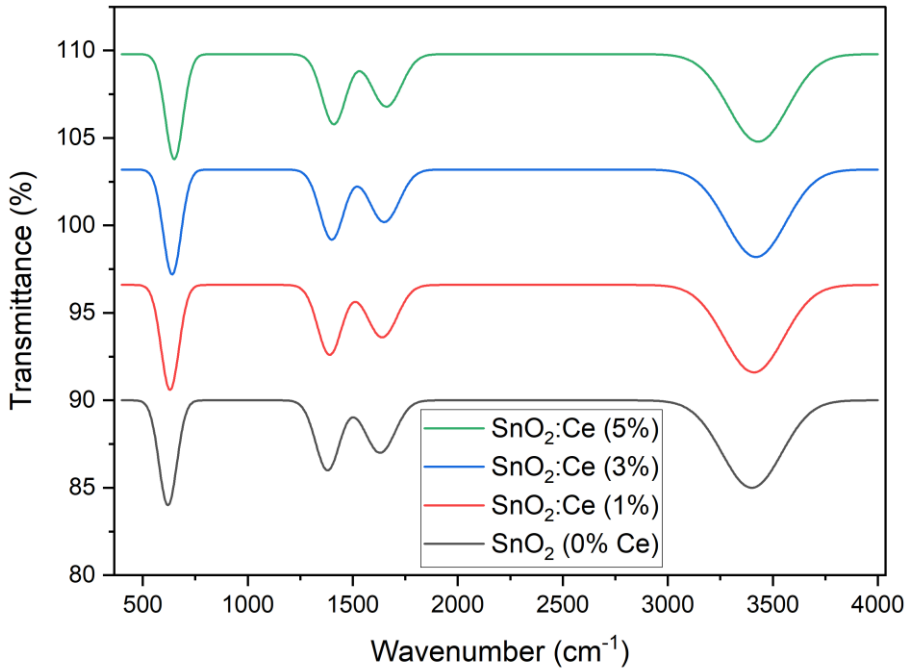

Figure 7 FTIR spectra of SnO_2 (0% Ce) and Ce-doped SnO_2 thin films (1%, 3%, and 5%) in the wavenumber range of 400–4000 cm^{-1}.

Table 4 FTIR absorption bands and corresponding vibrational assignments for SnO_2 and Ce-doped SnO_2 thin films prepared by spray pyrolysis.

Wavenumber region (cm^{-1})	Assigned vibration	Interpretation
620–670	Sn–O / Sn–O–Sn stretching	Confirms formation of SnO_2 lattice
1380–1450	Nitrate-related vibration / surface adsorbed species	Residual precursor species after deposition and annealing
1600–1650	H–O–H bending vibration	Adsorbed water or hydroxyl groups on film surface
3300–3500	O–H stretching vibration	Surface hydroxyl groups and adsorbed moisture

3.5.Electrical properties

The Hall effect measurements reveal that Ce doping has a pronounced influence on the electrical behavior of SnO_2 thin films. The electrical conductivity σ is inversely related to resistivity ρ through the relation $= \frac{1}{\rho}$, indicating that a reduction in resistivity results in enhanced conductivity. As presented in Table 5 and illustrated in Figure 8(a), the undoped SnO_2 film exhibits the highest resistivity (1.80×10^{-2} Ω·cm) and the lowest conductivity, which is attributed to its relatively low carrier concentration and limited defect-assisted conduction pathways. With the incorporation of Ce, the resistivity decreases significantly, reaching a minimum value of 4.20×10^{-3} Ω·cm for the SnO_2:Ce (3%) sample. Correspondingly, the conductivity increases to 238.10 $(\Omega\cdot cm)^{-1}$, as shown in Table 5 and Figure 8(a). This enhancement is mainly due to the increase in carrier concentration n, which contributes to conductivity according to the relation $\sigma = ne\mu$, where e is the elementary charge. The carrier mobility μ is calculated using the expression $= \frac{1}{\rho ne}$. As shown in Table 5 and Figure 8(b), the mobility increases from 2.89 $cm^2.V^{-1}.s^{-1}$ for pure SnO_2 to a maximum of 4.79 $cm^2.V^{-1}.s^{-1}$ for SnO_2:Ce (3%), indicating improved carrier transport and reduced scattering at this optimal doping level. This improvement can be attributed to enhanced crystallinity and reduced grain boundary resistance, which is consistent with the structural and morphological analyses (XRD and FESEM). The carrier concentration nnn increases progressively with Ce doping, rising from 1.20×10^{20} cm^{-3} for pure SnO_2 to 3.60×10^{20} cm^{-3} for SnO_2:Ce (5%), as shown in Table 5 and Figure 8(b). This behavior is associated with the presence of mixed valence states of cerium (Ce^{3+}/Ce^{4+}), which introduce donor levels and promote the formation of oxygen vacancies, thereby increasing the free electron density. However, at higher doping concentration (5% Ce), although the carrier concentration reaches its maximum, the mobility decreases to 2.55 $cm^2.V^{-1}.s^{-1}$, and the resistivity increases compared to the 3% Ce sample. This trend, clearly observed in Figure 8(a) and Figure 8(b), is attributed to increased ionized impurity scattering, defect density, and grain boundary effects, which hinder carrier transport. As a result, the conductivity decreases relative to the optimal SnO_2:Ce (3%) sample. A clear trend can be observed from Table 5 and Figure 8(a–b): Ce doping initially enhances electrical properties by increasing carrier concentration and mobility, leading to improved conductivity. However, beyond the optimal doping level (3% Ce), excessive dopant incorporation introduces structural defects and scattering centers that reduce mobility and overall electrical performance. Thus, SnO_2:Ce (3%) exhibits the best electrical characteristics, combining the lowest resistivity, highest conductivity, maximum mobility, and a high carrier concentration. This optimized balance makes it the most suitable composition for applications in transparent conducting electrodes, optoelectronic devices, and sustainable energy systems [8,11,33].

Table 5 Hall effect electrical parameters of SnO_2 and Ce-doped SnO_2 thin films, showing the variation of resistivity, conductivity, carrier concentration, and mobility with Ce concentration.

samples	ρ (Ω.cm)	σ $(\Omega.cm)^{-1}$	n (cm^{-3})	$\mu = \frac{1}{\rho * n * e}$ $(cm^2.V^{-1}.s^{-1})$
SnO_2 (0% Ce)	1.80×10^{-2}	55.56	1.20×10^{20}	2.89
SnO_2:Ce (1%)	9.50×10^{-3}	105.26	1.80×10^{20}	3.65
SnO_2:Ce (3%)	4.20×10^{-3}	238.10	3.10×10^{20}	4.79
SnO_2:Ce (5%)	6.80×10^{-3}	147.06	3.60×10^{20}	2.55

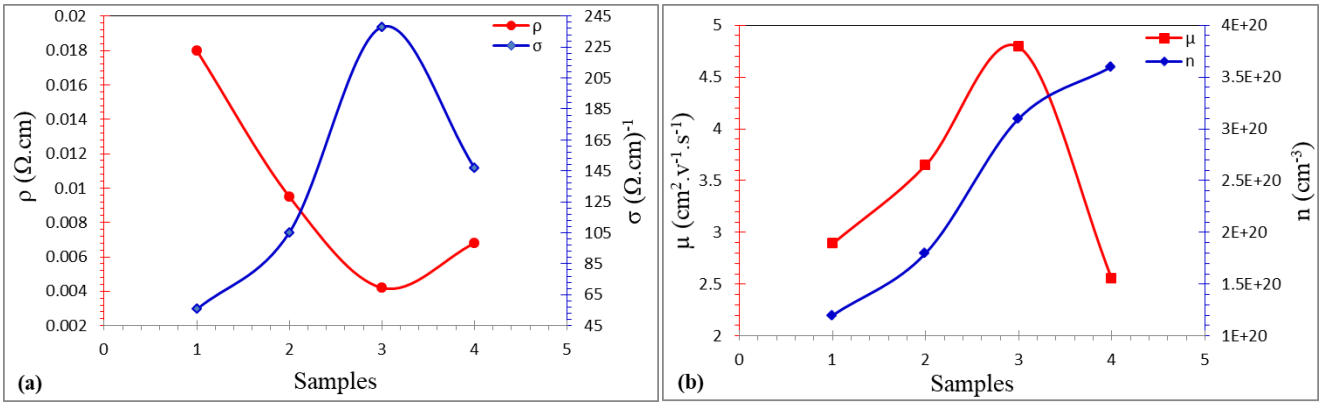

Figure 8 (a) Variation of resistivity (ρ) and conductivity (σ) as a function of Ce concentration in SnO_2 thin films. (b) Variation of carrier mobility (μ) and carrier concentration (n) with Ce doping.

4. CONCLUSIONS

In this study, pure and Ce-doped SnO_2 thin films (0%, 1%, 3%, and 5%) were successfully synthesized using the spray pyrolysis method and systematically investigated for their structural, morphological, optical, and electrical properties. XRD analysis confirmed that all films crystallize in the tetragonal rutile structure without the formation of secondary phases, indicating successful incorporation of Ce into the SnO_2 lattice. A gradual decrease in crystallite size and an increase in microstrain with increasing Ce concentration were observed, suggesting lattice distortion induced by dopant incorporation. FESEM and AFM analyses revealed that Ce doping significantly improves surface morphology by reducing particle size and surface roughness, leading to more uniform and compact films. The optimal morphology was achieved at 3% Ce doping, which exhibited the best balance between grain refinement and surface uniformity. Optical studies showed high transparency in the visible region for all films, with a slight reduction in transmittance and a red shift of the absorption edge upon Ce doping. The optical band gap decreased from 3.85 eV for pure SnO_2 to 3.65 eV for SnO_2:Ce (5%), as determined from Tauc plots, confirming band gap tuning due to defect states and oxygen vacancies. Hall effect measurements demonstrated that electrical properties were strongly influenced by Ce concentration. The conductivity improved significantly with doping, reaching a maximum at 3% Ce due to increased carrier concentration and mobility. However, further doping led to a decline in mobility due to enhanced scattering effects.

References

[1] A. A. Hateef, E. Dhahri, M. Rasheed, H. Kadhim, Z. Abbas, N. Hassan, Physics and Chemistry of Solid State, 25 (2024) 801. https://doi.org/10.15330/pcss.25.4.801-810
[2] A. Boumezoued, K. Guergouri, Régis Barillé, Rechem Djamil, Mourad Zaabat, M. Rasheed, J. Alloys Compd. 791 (2019) 550. https://doi.org/10.1016/j.jallcom.2019.03.251
[3] A. I. A. Ali, M. RASHEED, Experimental and Theoretical NANOTECHNOLOGY, 10 (2026) 277. https://doi.org/10.56053/10.s.277
[4] A. I. A. Ali, M. RASHEED, Experimental and Theoretical NANOTECHNOLOGY, 10 (2026) 239. https://doi.org/10.56053/10.s.239
[5] A. Jaber, M. Ismael, T. Rashid, M. A. Sarhan, M. Rasheed, I. M. Sala. Eureka: Phys. Eng. 4 (2023) 29. https://doi.org/10.21303/2461-4262.2023.002770
[6] A. Keziz, M. Heraiz, F. Sahnoune, M. Rasheed, Ceram. Int. 49 (2023) 32989. https://doi.org/10.1016/j.ceramint.2023.07.275
[7] A. Keziz, M. Heraiz, M. RASHEED, A. Oueslati. Mater Chem. Phys. 325 (2024) 129757. https://doi.org/10.1016/j.matchemphys.2024.129757
[8] A. Khaleefah, M. RASHEED, Experimental and Theoretical NANOTECHNOLOGY, 10 (2026) 289. https://doi.org/10.56053/10.s.289
[9] A. Kocyigit et al., "Highly efficient optoelectronic properties of SnO_2 thin films," J. Ovonic Res., 2012. https://doi.org/10.15251/JOR.2012.86.171
[10] A. R. J. Katae, H. H. Hussein, A. S. Jaber, M. A. Sarhan, M. RASHEED, Experimental and Theoretical NANOTECHNOLOGY, 10 (2026) 357. https://doi.org/10.56053/10.s.357
[11] A. R. J. Katae, H. H. Hussein, A. S. Jaber, M. A. Sarhan, M. RASHEED, Experimental and Theoretical NANOTECHNOLOGY, 10 (2026) 795. https://doi.org/10.56053/10.2.795
[12] A. Raghdi, M. Heraiz, M. Rasheed, A. Keziz, Journal of the Indian Chemical Society, 101 (2024) 101413. https://doi.org/10.1016/j.jics.2024.101413
[13] A. Zubaidi, L.M. Asaad, I. Alshalal, M. Rasheed, J. Mech. Behav. Mater. 32 (2023) 1. https://doi.org/10.1515/jmbm-2022-0302
[14] A.H. Ali, A.S. Jaber, M.T. Yaseen, M. Rasheed, O. Bazighifan, T.A. Nofal, Complexity 2022 (2022) 1. https://doi.org/10.1155/2022/9367638
[15] A.J. Hussein, M.N. Al-Darraji, M. Rasheed, M.A. Sarhan, IOP Conf. Ser.: Earth Environ. Sci. 1262 (2023) 022007. https://doi.org/ 10.1088/1755-1315/1262/2/022007
[16] A.J. Hussein, M.N. Al-Darraji, M. Rasheed, M.A. Sarhan, IOP Conf. Ser.: Earth Environ. Sci. 1262 (2023) 022005. https://doi.org/10.1088/1755-1315/1262/2/022005
[17] C. J. Brinker and G. Scherer, Sol-Gel Science, Academic Press, 1990. https://doi.org/10.1016/C2009-0-22386-5
[18] D. Batzill et al., "Defect chemistry in SnO_2," Phys. Rev. B, 2006. https://doi.org/10.1103/PhysRevB.73.165439
[19] D. Bouras, M. Rasheed, Opt. Quantum Electron. 54 (2022) 12. https://doi.org/10.1007/s11082-022-04161-1
[20] D. Kherifi, A. Keziz, M. Rasheed, A. Oueslati. Ceram. Int. 50 part A (2024) 30175. https://doi.org/10.1016/j.ceramint.2024.05.317
[21] E. Arif, R. Jamal, M. RASHEED, Experimental and Theoretical NANOTECHNOLOGY, 10 (2026) 453. https://doi.org/10.56053/10.2.453
[22] E. Kadri, K. Dhahri, R. Barillé, M. Rasheed. Phase Transi. 94 (2021) 65. https://doi.org/10.1080/01411594.2020.1832224

[23] F. Boudou, A. Belakredar, A. Berkane, M. Rasheed. Not. Sci. Biol. 17 (2025) 12183. https://doi.org/10.55779/nsb17212183
[24] F. Boudou, A. Guendouzi, A. Belkredar. M. Rasheed, Not. Sci. Biol. 16 (2024) 13837. https://doi.org/10.55779/nsb16211837
[25] F. Boudou, et al., Not. Sci. Biol. 17 (2025) 12593. https://doi.org/10.55779/nsb17312593
[26] F. Dkhilalli, S. M. Borchani, M. Rasheed, R. Barille, K. Guidara, M. Megdiche, J. Mater. Sci. Mater. Electron, 29 (2018) 6297. https://doi.org/10.1007/s10854-018-8609-z
[27] G. Frank and H. Köstlin, "Electrical properties of SnO_2," Appl. Phys. A, 1982. https://doi.org/10.1007/BF00616680
[28] H. K. Aity, E. Dhahri, M. Rasheed. Ceram. Int. 50 (2024) part B 54666. https://doi.org/10.1016/j.ceramint.2024.10.324
[29] H. K. Aity, M. Rasheed, E. Dhahri, A. A. Hateef, T. Saidani, Journal of Materials Science, 61 (2026) 6226. https://doi.org/10.1007/s10853-026-12241-w
[30] H. Kim et al., "Transparent electrodes," Appl. Phys. Lett., 1999. https://doi.org/10.1063/1.124353
[31] H. S. Akkera et al., "Structural and optical properties of doped SnO_2 films," Thin Solid Films, 2022. https://doi.org/10.1016/j.tsf.2022.139252
[32] I. Alshalal, H. M. I. Al-Zuhairi, A. A. Abtan, M. Rasheed, M. K. Asmail. J. Mech. Behav. Mater. 32 (2023) 1. https://doi.org/10.1515/jmbm-2022-0280
[33] I.M. Mohammed, M. Rasheed, AIP Conf. Proc. 3321 (2025) 020026. https://doi.org/10.1063/5.0289719
[34] J. Batzill and U. Diebold, "The surface and materials science of SnO_2," Prog. Surf. Sci., 2005. https://doi.org/10.1016/j.progsurf.2005.09.002
[35] K. Ellmer, "Resistivity of transparent conductors," Nat. Photonics, 2012. https://doi.org/10.1038/nphoton.2012.282
[36] L. L. Hench and J. K. West, "The sol–gel process," Chem. Rev., 1990. https://doi.org/10.1021/cr00099a003
[37] M. A. Sarhan, S. Shihab, B. E. Kashem, M. Rasheed, J. Phy.: Conf. Ser., 1879 (2021) 022122. https://doi.org/10.1088/1742-6596/1879/2/022122
[38] M. Enneffatia, M. Rasheed, B. Louati, K. Guidara, S. Shihab, R. Barillé, J. Phys.: Conf. Ser. 1795 (2021) 012050. https://doi.org/10.1088/1742-6596/1795/1/012050
[39] M. M. Najim, B. A. Yousif, M. RASHEED, Experimental and Theoretical NANOTECHNOLOGY, 10 (2026) 551. https://doi.org/10.56053/10.2.551
[40] M. M. Najim, B. A. Yousif, M. RASHEED, Experimental and Theoretical NANOTECHNOLOGY, 10 (2026) 627. https://doi.org/10.56053/10.2.627
[41] M. Rahman et al., "Comparative study of SnO_2 thin films," Mater. Sci. Appl., 2021. https://doi.org/10.4236/msa.2021.1212038
[42] M. Rasheed et al., J. Phys.: Conf. Ser. 1999 (2021) 012080. https://doi.org/10.1088/1742-6596/1999/1/012080
[43] M. RASHEED, A. Khaleefah, Materials Chemistry and Physics, 353 (2026) 132112. https://doi.org/10.1016/j.matchemphys.2026.132112
[44] M. Rasheed, et al., J. Adv. Biotechnol. Exp. Ther. 6 (2023) 495. https://doi.org/10.5455/jabet.2023.d144
[45] M. Rasheed, I. Alshalal, A.A. Ashed, M.A. Sarhan, A.S. Jaber, Indones. J. Electr. Eng. Comput. Sci. 33 (2024) 653. https://doi.org/10.11591/ijeecs.v33.i1.pp653-660
[46] M. Rasheed, M. N. Mohammedali, F. A. Sadiq, M. A. Sarhan, T. Saidani. J. Optics (New Delhi. Print) 54 (2024) 3490. https://doi.org/10.1007/s12596-024-01928-5

[47] M. Rasheed, M. Nuhad Al-Darraji, S. Shihab, A. Rashid, T. Rashid. J. Phys.: Conf. Ser. 1963 (2021) 012058. https://doi.org/10.1088/1742-6596/1963/1/012058
[48] M. Rasheed, M.N. Al-Darraji, S. Shihab, A. Rashid, T. Rashid, J. Phys.: Conf. Ser. 1963 (2021) 012059. https://doi.org/10.1088/1742-6596/1963/1/012059
[49] M. Rasheed, O. Alabdali, S. Shihab, A. Rashid, T. Rashid, J. Phys.: Conf. Ser. 1999 (2021) 012078. https://doi.org/10.1088/1742-6596/1999/1/012078
[50] M. Rasheed, O. Alabdali, S. Shihab, J. Phy.: Conf. Ser. 1879 (2021) 032120. https://doi.org/10.1088/1742-6596/1879/3/032120
[51] M. Rasheed, O.Y. Mohammed, S. Shihab, A. Al-Adili, J. Phys.: Conf. Ser. 1795 (2021) 012043. https://doi.org/10.1088/1742-6596/1795/1/012043
[52] M. Rasheed, R. Barillé, J. Non-Cryst. Solids., 476 (2017) 1. https://doi.org/10.1016/j.jnoncrysol.2017.04.027
[53] M. Rasheed, R. Barillé, Opt. Quantum Electron. 49 (2017). https://doi.org/10.1007/s11082-017-1030-7
[54] M. Rasheed, S. Shihab, O. Alabdali, A. Rashid, T. Rashid, J. Phys.: Conf. Ser. 1999 (2021) 012077. https://doi.org/10.1088/1742-6596/1999/1/012077
[55] M. Rasheed, SuhaShihab, O. Alabdali, H. H. Hassan, J. Phys. Conf. Ser., 1879 (2021) 032113. https://doi.org/10.1088/1742-6596/1879/3/032113
[56] M. Sellam, M. Rasheed, S. Azizi, T. Saidani. Ceram. Int. 50 (2024) 20917. https://doi.org/10.1016/j.ceramint.2024.03.094
[57] N. Assoudi et al. Opt. Quant. Electron. 54 (2022) 9. https://doi.org/10.1007/s11082-022-03927-x
[58] N. Ben Azaza et al., Opt. Mater., 96 (2019) 109328. https://doi.org/10.1016/j.optmat.2019.109328
[59] O. Alabdali, S. Shihab, M. Rasheed, T. Rashid. 3rd inter. Scient. conf. alkafeel univ. (ISCKU 2021) 2386 (2022) 050019. https://doi.org/10.1063/5.0066860
[60] P. Samarasekara et al., "Spin-coated thin films," Thin Solid Films, 2018. https://doi.org/10.1016/j.tsf.2018.04.042
[61] R. Banerjee et al., "SnO_2 nanostructures for energy," J. Mater. Chem., 2011. https://doi.org/10.1039/C1JM10607A
[62] R. Jalal, S. Shihab, M.A. Alhadi, M. Rasheed, J. Phys.: Conf. Ser. 1660 (2020) 012090. https://doi.org/10.1088/1742-6596/1660/1/012090
[63] R.S. Mahmood et al. J. Mech. Behav. Mater. 34 (2025) 1. https://doi.org/10.1515/jmbm-2025-0040
[64] S. Major and K. L. Chopra, "Indium tin oxide films," Thin Solid Films, 1983. https://doi.org/10.1016/0040-6090(83)90259-0
[65] S. Major et al., "Transparent conducting oxides," Thin Solid Films, 1986. https://doi.org/10.1016/0040-6090(86)90060-9
[66] S. Rani et al., "Sol–gel derived SnO_2 films," Ceram. Int., 2017. https://doi.org/10.1016/j.ceramint.2017.02.084
[67] S. S. Batros, M. Rasheed, H. K. Aity, A. A. Hatef, T. Saidani, Materials Chemistry and Physics, 355 (2026) 132243. https://doi.org/10.1016/j.matchemphys.2026.132243
[68] S. Shihab, M. Rasheed, O. Alabdali, A.A. Abdulrahman, J. Phys.: Conf. Ser. 1879 (2021) 022120. https://doi.org/10.1088/1742-6596/1879/2/022120
[69] T. Minami, "Transparent conducting oxide semiconductors," Semicond. Sci. Technol., 2005. https://doi.org/10.1088/0268-1242/20/4/R01
[70] T. Rashid, M. M. Mokji, M. Rasheed. J. Optics 54 (2024) 3490. https://doi.org/10.1007/s12596-024-02080-w

[71] T. Rashid, M.M. Mokji, M. Rasheed, J. Mech. Behav. Mater. 34 (2025) 77. https://doi.org/10.1515/jmbm-2025-0074
[72] T. Saidani, M. Rasheed, I. Alshalal, A.A. Rashed, M.A. Sarhan, R. Barillé, Res. Eng. Struct. Mater. 10 (2024) 743. http://dx.doi.org/10.17515/resm2023.21ma0922rs
[73] T. Saidani, S. Mokhtari, M. Rasheed, H. Lahmar, M. Trari, Journal of the Indian Chemical Society, 103 (2026) 102499. https://doi.org/10.1016/j.jics.2026.102499
[74] X. Chen et al., "Optical band gap tuning," J. Phys. D, 2014. https://doi.org/10.1088/0022-3727/47/15/153001
[75] Y. S. Lee et al., "Optical properties of SnO_2 thin films," Appl. Surf. Sci., 2018. https://doi.org/10.1016/j.apsusc.2018.01.123
[76] Y. Wang et al., "Tuning Electrical and Optical Properties of SnO_2 Thin Films," Coatings, 2025. https://doi.org/10.3390/coatings15060669
[77] Z. S. Ahmed, M. RASHEED, H. S. Ahmed, Experimental and Theoretical NANOTECHNOLOGY, 10 (2026) 329. https://doi.org/10.56053/10.s.329
[78] Z. S. Ahmed, M. RASHEED, H. S. Ahmed, Experimental and Theoretical NANOTECHNOLOGY, 10 (2026) 343. https://doi.org/10.56053/10.s.343
[79] Z. Zhang et al., "Rare-earth doped SnO_2 thin films," Mater. Lett., 2019. https://doi.org/10.1016/j.matlet.2019.01.056